Hierarchical Formation Mechanism of $CoFe_2O_4$ Mesoporous Assemblies

Carla Cannas,[*,†,‡] Andrea Ardu,[†,‡] Anna Musinu,[†,‡] Lorenza Suber,[§] Gabriele Ciasca,[∥] Heinz Amenitsch,[⊥] and Gaetano Campi[*,#]

[†]Dipartimento di Scienze Chimiche e Geologiche, Università di Cagliari, S.S. 554 Sestu, 009042 Monserrato, Cagliari, Italy, [‡]INSTM, Cagliari Unit, Università di Cagliari, S.S. 554 Sestu, 009042 Monserrato, Cagliari, Italy, [§]CNR-Istituto di Struttura della Materia, Via Salaria, Km 29.300, Monterotondo Stazione, RM I-00015, Italy, [∥]Istituto di Fisica, Università Cattolica del Sacro Cuore, Largo F. Vito 1, 00168, Roma, Italy, [⊥]Sincrotrone ELETTRA, S.S.14, km 163,5 in AREA Science Park, 34012 Basovizza, Trieste, Italy, and [#]CNR-Istituto di Cristallografia, Via Salaria, Km 29.300, Monterotondo Stazione, RM I-00015, Italy

ABSTRACT The development of synthetic hybrid organic−inorganic approaches and the understanding of the chemico-physical mechanisms leading to hierarchical assembly of nanocrystals into superstructures pave the way to the design and fabrication of multifunction microdevices able to simultaneously control processes at the nanoscale. This work deals with the design of spherical mesoporous magnetic assemblies through a surfactant assisted water-based strategy and the study of the formation mechanism by a combined use of transmission electron microscopy, X-ray diffraction, and time-resolved small angle X-ray scattering techniques. We visualize the hierarchical mechanism formation of the magnetic assemblies in the selected sodium dodecylsulfate (SDS)-assisted water-based strategy. At the first stage, an intermediate lamellar phase (L) represented by β-$Co(OH)_2$ and FeOOH hexagonal plates is formed. Then, the nucleation of primary $CoFe_2O_4$ (N_1) nanocrystals of about 6−7 nm occurs by the dissolution of FeOOH and the reaction of Fe^{III} ions coordinated to the SDS micelles, at the reactive sites provided by vertices and edges of the β-$Co(OH)_2$ plates. The intermediate phase consumes as the primary crystalline nanoparticles form, confined by the surfactant molecules around them, and assembly in spherical mesoporous assemblies. The key role of the surfactant in the formation of porous assemblies has been evidenced by an experiment carried out in the absence of SDS and confirmed by the pore size diameter of the assemblies (about 2−3 nm), that can be correlated with the length of the surfactant dodecylsulfate molecule.

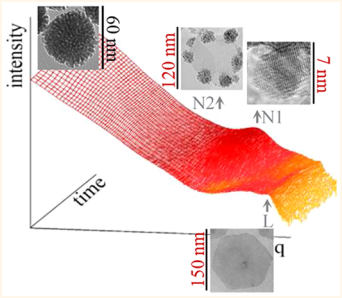

KEYWORDS: nanoparticle synthesis · mesoporous assemblies · spinels · surfactants · mechanism · *in situ* time-resolved SAXS

Mesoporous materials in the submicrometer and nanometer range with variable compositions, controllable size, morphologies, and pore structures are of particular interest for catalysis, adsorption, chromatography, bioseparation, and applications such as templates for nanomaterial synthesis.[1−4] For this reason, recently, the preparation of such materials has received much attention. Several authors report the achievement of spherical assemblies of primary nanocrystals made up of noble metals (Au, Pt, Ag, Pd, Rh),[5−9] nonmagnetic metal oxides[1,3] (titania, ceria, *etc*...) and magnetic oxides, mainly magnetite,[10−12] maghemite,[13] and spinel ferrites[14−17] but up to now no experimental evidence of the complex mechanism involved in the formation of the assemblies has been sorted out. Although magnetic particles with high magnetization values with a narrow size distribution have been synthesized through numerous methods, the products are overwhelmingly dominated by particles smaller than 30 nm.[18−26] However, for many purposes, it is preferable to fabricate larger nanoparticle assemblies up to 100 nm, because they can be easily moved by an ordinary external magnetic device.[27] It is therefore an interesting challenge to develop approaches to assembling magnetic nanoparticles with suitable sizes and morphology without compromising the surface area. Up to now, several methods have been developed to fabricate various superstructures from primary nanoparticles, among which, in particular, a number of methods are based on a surfactant-assisted strategy. Generally, a self-assembly mechanism is reported as the result of the spontaneous control of nanoentities that interplay through noncovalent interactions (hydrogen bonds, Van der Waal forces, electrostatic forces).[13,28−30] Mesoporous spherical aggregates of anatase nanocrystals have been fabricated using CTAB (cetyltrimethylammonium bromide)

* Address correspondence to ccannas@unica.it, gaetano.campi@ic.cnr.it.

Received for review April 10, 2015 and accepted July 1, 2015.

Published online July 01, 2015
10.1021/acsnano.5b02145

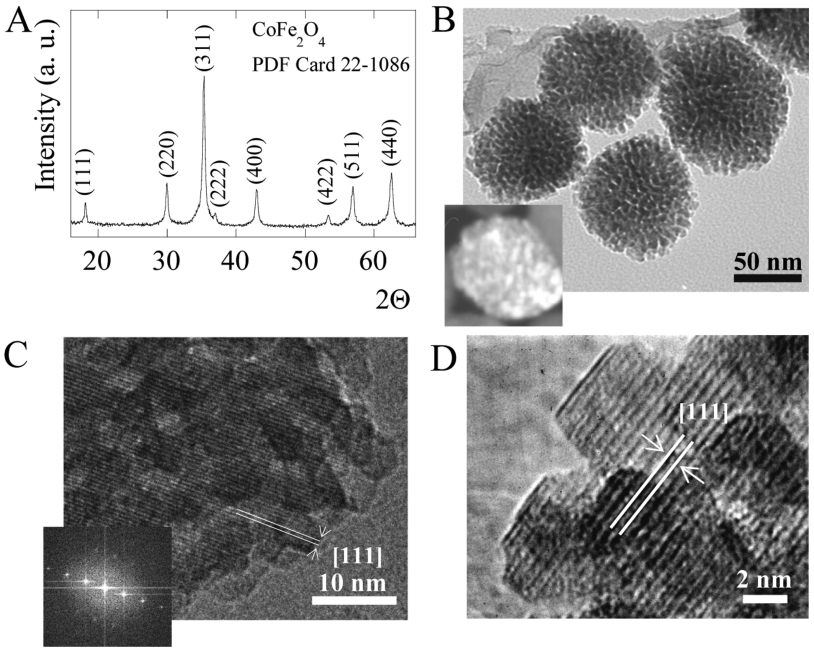

Figure 1. $CoFe_2O_4$ mesoporous assemblies synthesized at 80 °C and kept for 3 h: (A) XRD pattern; (B) TEM image (inset: dark field); (C,D) HRTEM images (inset: FFT).

as structure directing agent and the interaction between the solvent (cyclohexane) and the CTAB seems determinant to produce the assembly of 4−5 nm sized nanocrystals into spherical nanoporous aggregates.[31] Monodisperse spherical aggregates of CeO_2 nanocrystals have been obtained by the combined use of ionic liquid as template and solvent.[32]

In the literature, there are just a few works on magnetic spherical mesoporous assemblies. Magnetite spherical aggregates are reported by Jin who suggests as driving force for the assemblies the formation of $\pi-\pi$ interactions between primary nanocrystals.[33] The weak interaction among nanocrystals makes them easily destroyed by sonication. He *et al.*[34] justify the oriented aggregates of Co_3O_4 nanocrystals as the result of the binder effect of water molecules and the capping effect of the alcohols groups on the nanocrystal surface. Hu *et al.*[35] report the spherical nanoparticle assemblies formation due to the presence of a ternary surfactant whereas Rotello *et al.*[36] introduced a functionalized polystyrene as the "mortar" for nanoparticle assemblies. Euliss *et al.*[13] report the use of block copolypeptide to induce the formation and the stabilization of small clusters of preformed hydrophilic maghemite nanocrystals.

Here, on the basis of a simple and versatile one-pot surfactant-assisted reaction in water, we investigate the reaction mechanism with the combined use of different techniques. The aim is to find out an experimental response to understand the formation mechanism of iso-oriented spherical $CoFe_2O_4$ mesoporous assemblies.

RESULTS AND DISCUSSION

$CoFe_2O_4$ Mesoporous Assemblies. $CoFe_2O_4$ powder obtained at 80 °C and kept at this temperature for 3 h has been characterized by wide angle X-ray diffraction (XRD) and transmission electron microscopy (TEM) measurements. In Figure 1A the X-ray powder diffraction pattern shows Bragg reflections which, on the basis of their position and relative intensity, can be unequivocally indexed as cubic spinel ferrite ($CoFe_2O_4$, PDF Card 22-1086). No peaks of other phases are detected. According to the Scherrer formula, the average crystallite size was calculated on the (220) reflex and resulted to be 22 ± 1 nm. Figure 1 panels B−D and insets show representative TEM micrographs at low and high magnification. It can be clearly seen that the sample is composed of 50−80 nm in size mesoporous spherical assemblies of small nanocrystals (Figure 1B and inset, see white spots in the dark field image). The spherical assemblies are stable and keep their shape and size unchanged also after the washing procedures and intense and prolonged ultrasound irradiation. The images in high-resolution mode, Figure 1C and Figure 1D, show spherical assemblies made of small primary nanocrystals (about 7 nm in size) and a worm-like nanopores structure with a pore size of about 2−3 nm. The parallel lattice fringes are uniformly extended over the primary building blocks (Figure 1C), the grain boundaries, and the nanopores. The primary nanocrystals are organized into an iso-oriented attachment structure through sharing identical lattice planes. The lattice plane distance of 4.8 Å was calculated from the image and corresponds to the [111] reflex of the cubic spinel phase. The iso-oriented structure is further confirmed by the FFT image (inset Figure 1C) that shows symmetrically aligned spots like satellite reflections caused by double diffraction. The image at a higher magnification (Figure 1D) reveals that the

primary crystals are square-shaped, and a more careful observation evidenced in our previous work[15] shows that two or three particles share edges form twin crystals, which is consistent with the symmetrical double spots present in the FFT. This justifies the apparent disagreement between the $CoFe_2O_4$ average crystallite size (22 nm) obtained by XRD and the average crystal size (6−7 nm) extracted from TEM data. Nitrogen adsorption−desorption isotherms indicate mesopores sizes of about 2−3 nm, consistent with TEM results. The surface area of the assemblies is 160 m^2/g, in good agreement with the theoretical value calculated by assuming dense and regular $CoFe_2O_4$ cubes sharing edges of 6−7 nm.[15]

Kinetics: Reaction and Assemblies Formation Mechanism. To study the mechanism involved into the formation of the spherical assemblies, TEM and XRD analyses performed at different times of the reaction have been accompanied by *in situ* and time-resolved SAXS measurements.[37,38]

TEM. TEM and high resolution TEM (HRTEM) analyses on the $CoFe_2O_4$ sample at 80 °C after 3, 6, 12, 20, and 30 min of reaction were carried out, and the results are shown in Figure 2. The bright field image of the sample at 3 min shows a great deal of hexagonal platelet crystals of average diameter in the 100−250 nm range and thickness of about 7−9 nm (Figure 2D). At the same time at the edges of some of the hexagonal platelets, and often at the corners, are clearly visible small assemblies of nanocrystals in the 20−40 size range. There is no evidence of free single primary nanocrystals nor assemblies, all of these being attached to the hexagonal platelets. This indicates that the spherical assemblies are formed at the earliest stages of the synthesis from the hexagonal platelets. Bright Field images of the sample at 6 and 12, 20, and 30 min show the evolution of the reaction; the number of the spherical assemblies increases and, at the same time, the hexagonal platelets are worn out gradually up to be almost completely consumed (30 min).

XRD. XRD patterns of the samples at 3, 6, 12, and also 30 min, reported in Figure 3A, show besides the typical reflections of the cubic spinel ferrite an intense large peak at about 19° accompanied by two other low-intensity peaks at about 40° and 54°. The peak position at 19° is in good agreement with the presence of β-$Co(OH)_2$ (PDF Card 74-1057) and/or $Fe(OH)_2$ (PDF Card 13-0089) which are isostructural. The absence of other reflections of these phases could indicate a preferred orientation of the crystals, consistently with the peculiar platelet shape observed by TEM, as reported also by other authors for β-$Co(OH)_2$.[39] The coherent domain calculated by the Scherrer equation on the peak at 19° ((001) reflex) is about 9 nm, still in good agreement with the thickness of the platelets revealed by TEM images (Figure 2D) . The two other weak peaks at about 40° and 54° (see Figure 3B, a detail of the XRD pattern at 3 min) could be an indication of the presence of the δ-FeOOH phase (PDF Card 77-0247). The amount of the spinel phase with respect to the β-$Co(OH)_2$/$Fe(OH)_2$ increases with reaction time and after 30 min the hydroxide−oxide transition is completed. In all the samples at 3, 6, 12, and 30 min, as well as in the final one (3 h, Figure 1A) the spinel phase crystallite size calculated on (220) reflection is about 22 nm indicating that primary nanocrystals form at the early stage of the synthesis and do not grow with time. However, the number of $CoFe_2O_4$ nanoparticles increases with time at the expense of the hydroxy-oxy phases, as observed from the increase of the reflection intensities associated with the spinel phase, and at the same time the self-assembly process continues at least up to 12 min and consequently the size of the spherical aggregates increases. To clarify the formation mechanism of these $CoFe_2O_4$ mesoporous assemblies, two samples prepared in the same conditions but in the absence of sodium dodecyl sulfate ($CoFe_2O_4$_NS) or in the absence of cobalt (Fe_2O_3) were synthesized. Figure 3 reports XRD (C,D and E,F) and TEM (G,H and I,L) data. The XRD pattern of $CoFe_2O_4$_NS evolution with time (Figure 3C) follows a trend similar to that observed for the sample synthesized in the presence of SDS: $CoFe_2O_4$, β-$Co(OH)_2$/$Fe(OH)_2$ and δ-FeOOH (Figure 3D, a detail of the XRD pattern at 3 min) are present from the early stages of the synthesis. The broad reflection at about 19° associated with the $Me^{II}(OH)_2$ indicates the formation of very small nanocrystals, and as a consequence, at 3 min a higher percentage of $CoFe_2O_4$ phase is formed suggesting a higher reactivity if compared with the sample prepared with SDS. TEM data confirm these results. Figure 3G shows the coexistence of very thin layers (arrows), in agreement with the XRD broad reflection at 19°, accompanied by a great number of dark nanoparticles with high size polydispersity, easily associable to the ferrite phase. After 30 min, the evolution to the final phase is complete and only nonporous roughly hexagonal nanocrystals (Figure 3H and inset dark field) of about 100 nm are present. These results prove that the surfactant has a key role on the spherical mesoporous assemblies formation. The DS chains probably interact with the surface of the forming spinel during the assembly growth preventing the collapse of the structure into a single nanocrystal. To confirm the presence of δ-FeOOH, of which the reflections in the XRD pattern are very weak, the synthesis was performed also in the absence of cobalt. XRD patterns (Figure 3E,F) point out, once again, the presence of a spinel phase, that in this case can be attributed clearly to the maghemite (γ-Fe_2O_3) phase (PDF Card: 25-1402), isostructural with $CoFe_2O_4$, accompanied by a phase characterized by the presence of two very weak peaks that can be associable to δ-FeOOH (PDF Card 77-0247). The actual proof of the δ-FeOOH presence is given by TEM,

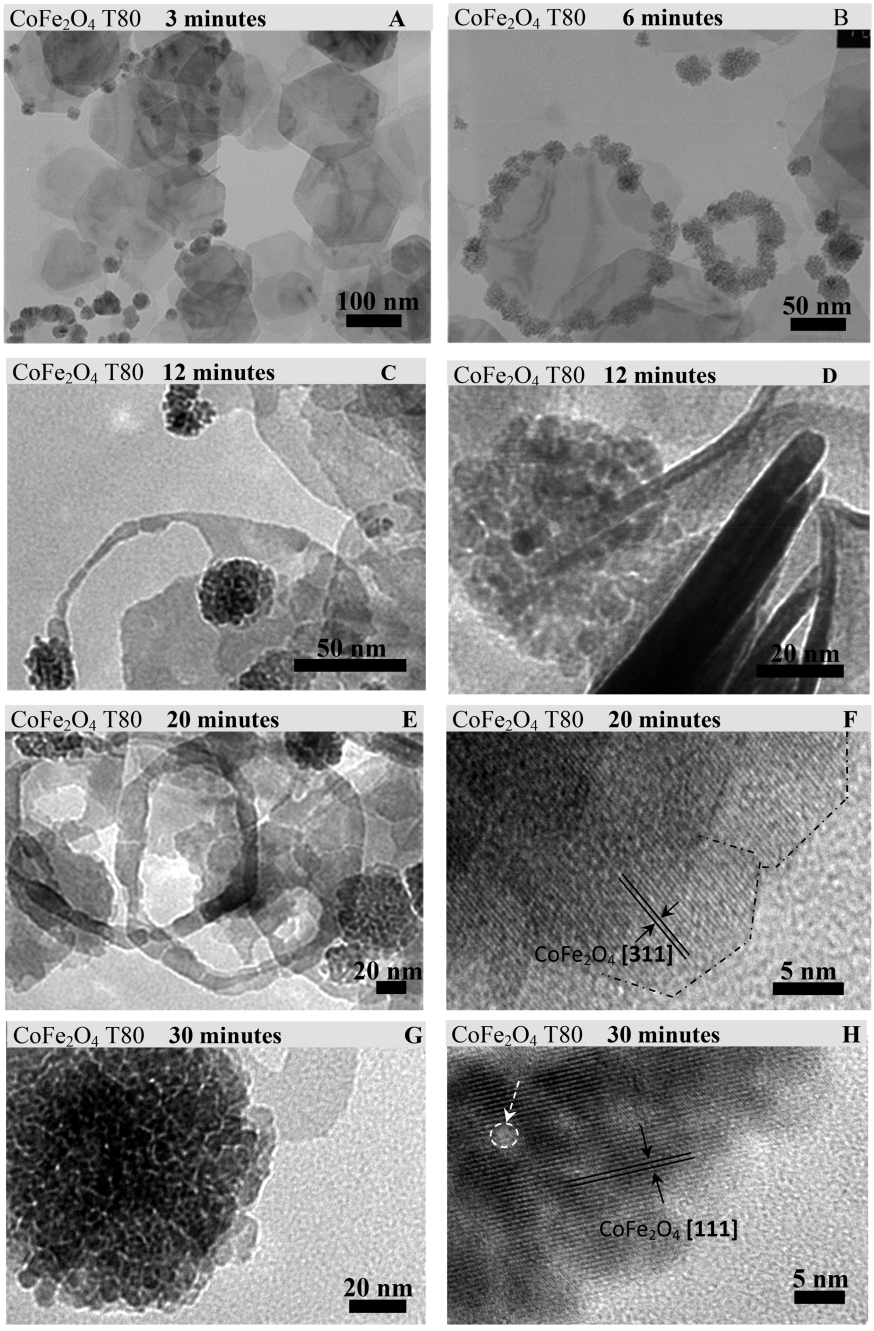

Figure 2. TEM images of the samples prepared at 80 °C blocking the reaction at 3 min (A), 6 min (B), 12 min (C and D), 20 min (E, F), and 30 min (G, H).

the sample at 3 min being made up of very thin hexagonal platelets, similar in shape and size to the ones observed in the case of the $CoFe_2O_4$ systems at the same reaction time (Figure 3l). Furthermore, XRD and TEM data allow the exclusion of the presence of $Fe(OH)_2$, hypothesized as a possible intermediate for the formation of the final phase. In fact, in this case (in the absence of cobalt), the $Fe(OH)_2$ main reflection falling at 19° is absent. As a consequence, the reflection at 19° observed for $CoFe_2O_4$ systems up to 12 min ($CoFe_2O_4$ and $CoFe_2O_4$_NS) is only ascribable to β-$Co(OH)_2$. This result is expected considering our synthetic condition ($FeCl_2$ aqueous solution, pH = 12, temperature of 80 °C, air). In fact, it is reported in the literature that the use of $FeCl_2$ in an aqueous alkaline medium (pH > 8) at room temperature in air, leads to a rapid Fe^{II} oxidation, possibly to δ-FeOOH (PDF Card 77-0247).[40,41] Moreover, the $Fe(OH)_2 \Rightarrow \delta$-FeOOH transition can be considered a topochemical transformation. In fact, $Fe(OH)_2$ and δ-FeOOH possess similar crystal planes and the {001} facets of $Fe(OH)_2$ (d = 4.60 A) match well with {001} facets of δ-FeOOH ((d = 4.53 A).[42] In our synthetic conditions, the higher pH and temperature may induce this transition to be so rapid that it cannot be

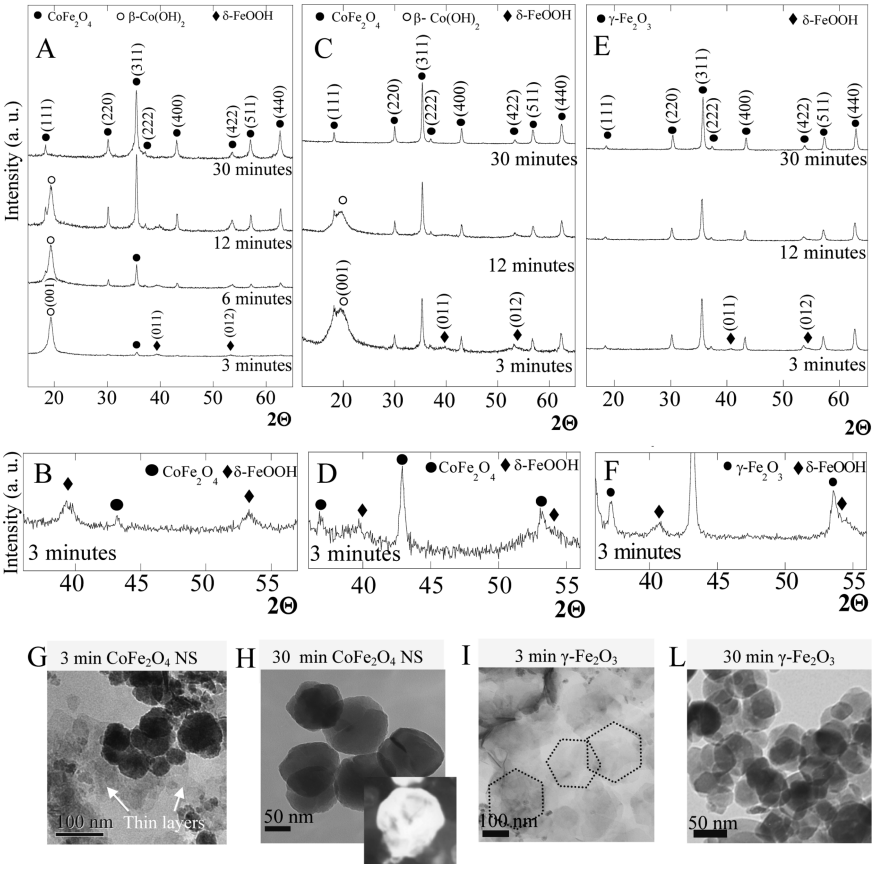

Figure 3. XRD patterns of the samples prepared in the presence of SDS, ($CoFe_2O_4$) (A,B), in the absence of SDS ($CoFe_2O_4$ NS) (C,D) and in the absence of cobalt, γ-Fe_2O_3 (E,F). TEM images of the sample $CoFe_2O_4$ NS at 3 min (G) and 30 min (H and inset dark field) and of the sample γ-Fe_2O_3 at 3 min (I) and 30 min (L).

experimentally observed, and only β-$Co(OH)_2$ and δ-FeOOH coexist as intermediate to $CoFe_2O_4$ mesoporous spherical assemblies.

Time-Resolved SAXS Measurements. SAXS patterns have been collected on $CoFe_2O_4$ nanoparticles synthesized through the formation of normal micelles using sodium dodecyl sulfate (SDS) as surfactant with the following main steps: (1) Aqueous solutions of $CoCl_2$ and $FeCl_2$ in a 1:2 molar ratio have been added in aqueous solutions of SDS in a glass flask and stirred constantly, for 30 min. (2) Methylamine solution, heated at the same temperature, has been added.

During step 1, SAXS patterns have been collected on the SDS solution, on the $FeCl_2$ and SDS solution (after the addition of the $FeCl_2$) and on the $CoCl_2$ + $FeCl_2$ + SDS aqueous solution (after the introduction of the $CoCl_2$). The SAXS profiles in the subsequent substeps of (1), shown in Figure 4, have been modeled with core−shell ellipsoids, as in Narayanan et al.[43] The least-squares fitting procedure gives an inner core radius of 1.54 and 2.45 nm with a shell thickness of 0.61 nm (see inset of Figure 3). The addition of iron and cobalt chlorides does not induce any significant modification in core−shell ellipsoid size, suggesting the formation of $Na_xFe_yCo_z(DS)_n$, micelles rich in Na ($x > y$ and z). This is in agreement with the use of a high

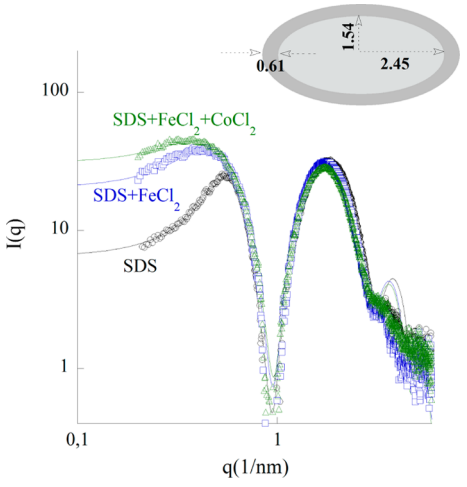

Figure 4. SAXS patterns of the of SDS, SDS + $FeCl_2$, and SDS + $FeCl_2$ + $CoCl_2$ aqueous solution, after water background subtraction, along the modeled curves (dotted lines).

amount of SDS during the synthesis. Unlike the size, the interactions of the core−shell ellipsoids change with the ions addition. Indeed, the structure factor $S(q)$ for SDS micelles, calculated using rescaled mean spherical approximation (RMSA), decreases with the presence of the metal salts, indicating the development of a shield effect making the micelles more diluted in the

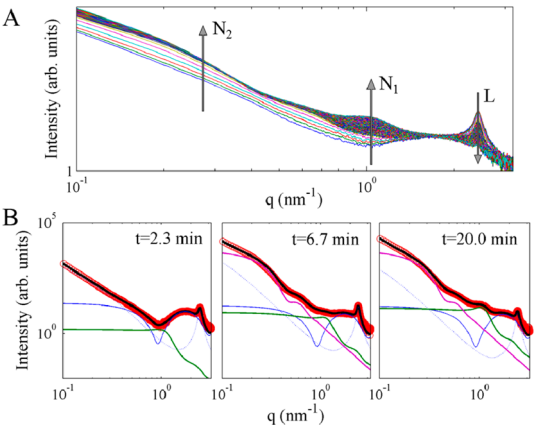

Figure 5. (A) SAXS patterns collected during the reaction at T = 80 °C after water background subtraction. The arrows indicate the q-range where we observe the growth of primary particles, N_1, the aggregates N_2, and the consumption of the intermediate lamellar phase, L. (B) Experimental SAXS patterns (red circles) along the best fitting curves (black lines) at the different indicated times during the reaction. The profiles of the different contributions in the model of eq 1 given by I_{SDS} (blue line), I_{IL} (dotted blue line), I_{N_1} (green line), and I_{N_2} (dotted magenta line), are reported.

solution. To understand the growth kinetics of the primary particles and their aggregation in mesoporous assemblies, *in situ* time-resolved SAXS measurements have been performed at two different temperatures. Time evolution of SAXS profiles at T = 80 °C, after background subtraction, are shown in Figure 5A. We can distinguish different q-ranges associated with different phases, as indicated by the arrows. More specifically, the total scattered intensity, I, can be modeled as

$$I = I_{SDS} + I_L + \sum_{i=1}^{i=2} I_{Ni} + I_A \qquad (1)$$

I_{SDS} is associated with the SDS and Me(DS)n micelles; I_L represents an intermediate lamellar phase, L, composed by large hexagonal flat particles as indicated by the TEM images shown in Figure 2.

The intermediate phase, L, has been modeled as large planar objects giving the intensity I_{La}, given by

$$I_{La}(q) = N_L \eta \frac{2(\pi D/2)^2}{(qD/2)^2[1 - J(qD)/(qD/2)]} \times \int_0^\infty L\left(\frac{\sin(qT_L/2)}{qT_L/2}\right)^2 P_{SZ}(q, T_L)\, dT_L\, dq \qquad (2)$$

D and T_L in (2) represent the largeness and the thickness of the planar objects. N_L and η are the particle density number and contrast between the solution and the scattering large objects; $J(qD/2)$ is the generalized Bessel function calculated at the first order. The distribution of the thickness, T_L, of these planar objects has been taken into account by integration of the intensity over a Schutz−Zimm probability distribution given by

$$P_{SZ}(q, T_L) = \frac{1}{T_{Lm}}\left(\frac{T_L}{T_{Lm}}\right)^{k-1} k^k \exp\left[-\frac{kT_L/T_{Lm}}{\Gamma(k)}\right] \qquad (3)$$

where T_{L_m} is the mean of the distribution and $k = 1/S_g^2$ where S_g is the standard deviation of the distribution, associated with the particles polidispersity. The lamellar peak at $q = q_0 = 2.4\ nm^{-1}$ has been fitted by a Lorentzian function I_{Lp}:

$$I_{Lp}(q) = \frac{A}{1 - (q - q_0\sigma)^2} \qquad (4)$$

taking into account the lamellar character of the intermediate phase, L; q_0 and σ represent the center and the width of the Lorentzian peak, respectively.

The term

$$\sum_{i=1}^{i=2} I_{N_i}$$

in eq 1 represents two populations of spherical particles, namely N_1 and N_2, modeled as

$$I_{N_i}(q) = N(i)S(q, R_{HS}(i), f_p(i), \tau(i)) \times \int_0^\infty P_{SZ}(i)_{SZ}(q, R(i))[f_{sphere}(q, R(i))]^2\, dR \qquad (5)$$

with i = 1, 2 and where $N(i)$ is the particles number in the i population with radius $R(i)$; to account for the polydispersity of the particles, the intensity has been integrated over a Schutz−Zimm distribution of R, for each population. The interactions of primary particle N_1 taking place in the aggregation process, have been modeled in the monodisperse approximation of sticky hard spheres with radius R_{HS} and volume fraction f_p.[44] The stickiness parameter τ, characterizing the adhesive strength is found to be constant during the reaction. The last term, I_A, in eq 1 taking into account large assemblies (larger than 30−40 nm in size), is set as a power-law background given by $I_A = P_c q^{Pe}$. SAXS profiles have been modeled by eq 1 using the trust-region-reflective least-squares algorithm.[45,46] The fitting procedure allowed us to estimate the number density N_L and thickness T_L of the intermediate lamellar phase (L), the number density N, the mean radius R_m, and the dispersivity S_g of the Schutz−Zimm $P_{SZ}(R)$ size distribution of primary particles (N_1 population) and secondary nanoparticles (N_2 population). Since the standard for absolute calibration did not give trustful results, the intensity scale of particle number densities are expressed in arbitrary units. For each parameter, the corresponding confidence interval was also estimated. Fits with the included contributes, I_{SDS}, I_L, I_{N_1} and I_{N_2} in eq 1, obtained at different times are shown in Figure 5B. We can observe that the SDS contribution remains nearly constant during the reactions, suggesting its *template* role as dispersant padding of the primary nanoparticles N_1. The intermediate lamellar phase L gradually decreases, during the formation of the primary particles N_1 and of the secondary nanoparticles N_2. Color maps of the SAXS profiles intensity, as a function of time, of the different phases L, N_1 and N_2, are shown in Figure 6. Size distributions, $P_{SZ}(q,R)$, of

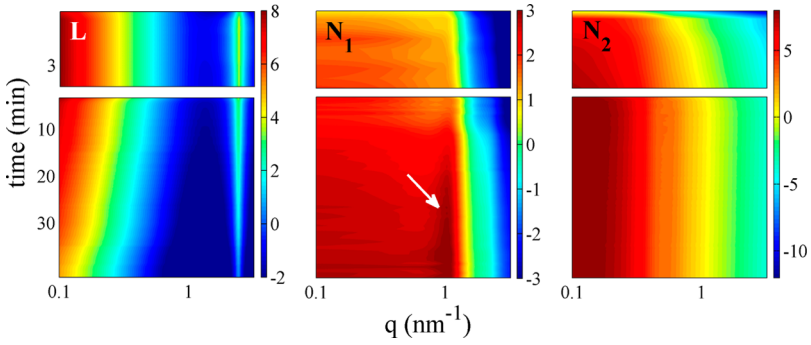

Figure 6. Maps of the SAXS profiles of L, N_1, and N_2 populations as a function of time, during the reaction. Each map has been divided in two parts separated by the white stripes; the lower parts indicate the consumption of the intermediate lamellar phase. The peak at $q = 1.0$ nm^{-1} in the N_1 maps, indicated by the white arrow, is due to the increasing volume fraction, f_p, in eq 5; it denotes the interactions between primary particles taking place as soon as the assembly (N_2) starts.

the two populations N_1 and N_2, at $T = 80$ °C are shown in Figure 7. The size of the N_1 nuclei, given by $2R_m(1)$, is found to be 5.0 ± 1.2 nm with a polydispersity of about 15%. This is consistent with TEM data, and remains nearly constant during the reaction. The formation of N_1 primary particles is followed by the formation of secondary particles (N_2 population). The N_2 formation is associated with the appearance of the correlation peak at $q = q_{HS} = 1$ nm^{-1} in the structure factor $S(q, R_{HS}(1), f_p(1), \tau(1))$, indicated by the white arrow in the N_1 growth map of Figure 6. The interparticle distance, R_{HS}, between primary particles and the volume fraction, f_p, are shown in the panel A of Figure 7. We found a size of $2R_m(2) = 20.0 \pm 2.2$ nm for secondary nanoparticles in N_2 population. This value is in good agreement with XRD data that evidenced crystallites of 22 nm and justified by TEM analysis as made up of three primary cubic nanoparticles sharing edges and forming twin crystals.[15] The reaction kinetics can be described by the time dependence of the total volume

$$V = N \int_0^\infty P_{SZ}(R, q) v(R)\, dR \qquad (6)$$

of L, N_1, and N_2 phases in model (1); $v(R)$ is the volume of the single particle, $4/3\pi R^3$ for the spheres in populations N_1 and N_2 and $\pi R^2 L$ for the large planar objects of the intermediate lamellar phase. In panel B of Figure 7 we show the total volumes of the intermediate L, N_1, and N_2 populations. The formation of the intermediate phase composed of cobalt hydroxide plates with thickness T_L of about 7 nm, occurs in the $\Delta t_1 = 2.2$ min early stage, just after the methylamine addition. As the L phase develops, primary particles with size $2R_m$ similar to β-$Co(OH)_2$ plates' thickness (6−7 nm) start to form. The constant size of primary particles could indicate that the hexagon edges constitute the sites for their nucleation; these hexagonal edges could also give the crystalline twin observed in electron diffraction data.[15] The periodicity of the lamellar intermediate phase L corresponds to $2\pi/q_0 = 2.61 \pm 0.08$ nm where q_0 is the center (see eq 3) of the Lorentzian peak, I_{Lp}. This value is consistent with the diagonal of the face in the cubic

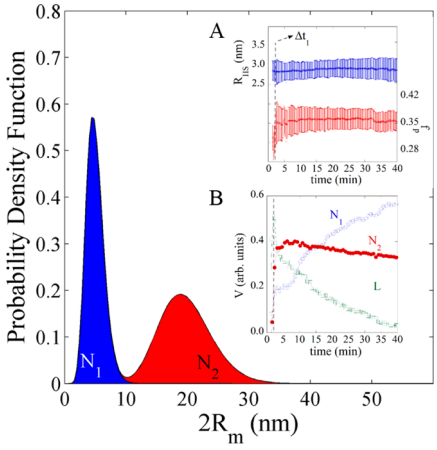

Figure 7. Schultz−Zimm distributions, $P_{SZ}(R)$, of the size of primary particles (N_1 population) and spherical assemblies (N_2 population). The inset (A) shows the time evolution of the interparticle distance, R_{HS}, and the volume fraction f_p with their uncertainness ΔR_{HS} and Δf_p, in the N_1 population during the reaction. At the Δt_1 time, the assembly takes place. The total volumes of the L, N_1, and N_2 populations calculated by eq 6 are reported in the inset (B).

cell of the crystal spinel structure. In Figure S1 we can appreciate the second order peak in the higher resolution SAXS spectra.

During the primary particles nucleation and assembly, the intermediate phase decreases until it is consumed in about 30 min. In this range the N_2 population forms. We observe a decreasing of the N_2 total volume due to the formation of the final assemblies with sizes larger than 40 nm.

To get further insight on the growth kinetics of the primary particles and their aggregation in mesoporous spherules, *in situ* time-resolved SAXS measurements have been performed also at $T = 50$ °C using the same experimental setup (see SI). At this lower temperature, we find a slower kinetics leading to different size and dispersity of mesoporous spherules. This suggests the possibility of using different temperatures reactions to control the evolution of the different L, N_1, and N_2 phases. In this way we open easy routes for tuning structural nanoparticles parameters, such as size and

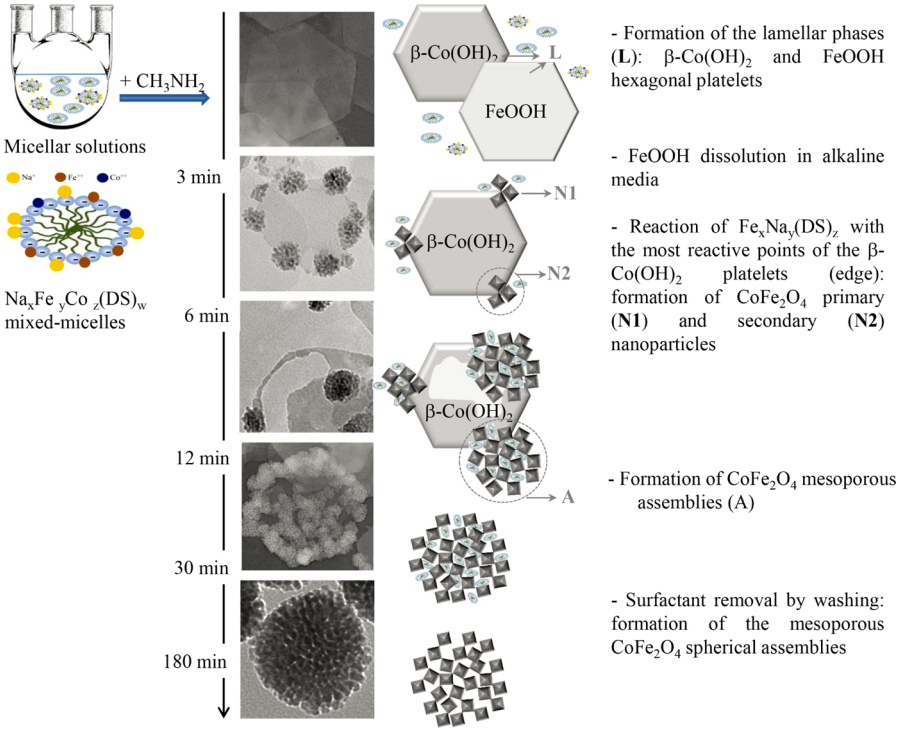

Figure 8. Schematic representation of the hierarchical formation mechanism of $CoFe_2O_4$ mesoporous assemblies.

dispersity.[47] The results are shown in detail in Figure S2 together with TEM and XRD data reported in Figure S3 of the Supporting Information.

CONCLUSIONS

This work deals with the design of $CoFe_2O_4$ spherical mesoporous assemblies and the study of the formation mechanism by a multitechnique approach that consists on the combined use of TEM and XRD accompanied by in situ time-resolved SAXS techniques. By way of time-resolved SAXS measurements we find that at the first stage a $Na_xMe_y(DS)_z$ micellar solution coexists with a lamellar phase. TEM and XRD analyses have permitted the association of this lamellar phase (L) to β-Co(OH)$_2$ and FeOOH hexagonal plates. The evolution with time in SAXS patterns evidence the formation of three different entities that correspond to the formation of primary $CoFe_2O_4$ nanocrystals (N_1), secondary nanoparticles made up of three primary nanoparticles (N_2) grown on the lamellar phase edges, and $CoFe_2O_4$ spherical assemblies (A) at the expenses of the lamellar phase that gradually disappears. This is in agreement with TEM and XRD measurements that clearly show that the spinel phase forms and grows on the hexagonal platelets starting from their corners or edges (the most reactive zones). In particular, the formation of the spinel phase probably derives from the reaction of iron(III) released from dissolution of δ-FeOOH in strongly alkaline media and probably present as $Fe_xNa_y(DS)_z$ micelles, with the β-Co(OH)$_2$ plates, which, as a consequence, are gradually consumed. (Figure 8) The surfactant has a key role on the creation of mesopores, as confirmed by an experiment carried out in the absence of SDS. SAXS measurements suggest that the formation mechanism can be kinetically controlled by the reaction temperature, able to modify the speediness of the reaction, affecting both the size distribution of primary particles and the size of their mesoporous assemblies. SAXS measurements provide a powerful and exhaustive tool to visualize the peculiar hierarchical mechanism leading to the formation-organized worm-like mesoporous structures opening the possibility to extend the surfactant-assisted water-based strategy set up for $CoFe_2O_4$ mesoporous to the class of materials known as spinel ferrites.

MATERIALS AND METHODS

Chemicals. $CoCl_2 \cdot 6H_2O$ (98%), $FeCl_2 \cdot 4H_2O$ (≥99%), SDS (98%), CH_3NH_2 (40% w/w) were purchased from Sigma-Aldrich and used as received.

Synthesis. $CoFe_2O_4$ nanoparticles were synthesized through the formation of normal micelles using sodium dodecyl sulfate (SDS) as surfactant following a procedure described in our previous works.[15,16] Aqueous solutions containing $CoCl_2$ $6H_2O$ (50 mL, 0.005 mol) and $FeCl_2$ $4H_2O$ (50 mL, 0.01 mol) in a 1:2 molar ratio were added to 190 mL of an aqueous solution of SDS (0.06 mol) and stirred constantly at room temperature for 30 min. An amount of SDS, twice as high as the stoichiometric one, was used. As a result, this micellar solution should be composed initially of sodium(I), cobalt(II), and iron(II) mixed micelles. The reaction flask was dipped in an oil bath at 80 °C, constantly mechanically stirred, and 10 mL of methylamine

solution heated at the same temperature was added. The solution became green, and after a few minutes the color changed to dark brown. The dark slurry was stirred for 3 h and then cooled to room temperature. The precipitate was isolated by decantation and centrifugation. The nanoparticles were washed several times with diluted ammonia to remove the surfactant excess. Finally the $CoFe_2O_4$ powder ($CoFe_2O_4$) was dried overnight in an oven at 70−80 °C. Two other experiments were carried out in the same synthetic condition but in the absence of cobalt (γ-Fe_2O_3 nanoparticles) and in the absence of SDS ($CoFe_2O_4$ _NS) in order to investigate on the mechanism of the assemblies formation.

To study the kinetic of the reaction, samples were taken at selected times (portions of 20 mL of the dispersion) and poured into a beaker containing 80 mL of water at room temperature and immediately separated by centrifugation.

Characterization Techniques. TEM analysis was performed immediately on a drop of the dispersion taken at the selected time and deposited onto the TEM grid. The suspensions were dropped on carbon-coated copper grids for the TEM observations with a TEM (JEOL 200CX, operating at 200 kV). High resolution TEM images were obtained with a JEM 2010 UHR equipped with a Gatan Imaging Filter (GIF) with a 15 eV window and a 794 slow scan CCD camera.

The samples were characterized by XRD, using a Seifert diffractometer with a Bragg−Brentano geometry with Cu Kα wavelength. *In situ* time-resolved spectra have been collected on the SAXS beamline at the ELETTRA synchrotron light source following the reaction in continuum, at 80 and 50 °C.[37,38] The reaction solution in a glass flask in a thermostated batch reactor apparatus was monitored by way of time-resolved SAXS; a remote controlled syringe allowed us to add 10 mL of methylamine aqueous solution into the reaction solution and a peristaltic pump continuously flowed the solution mixture in a 1.5 mm quartz capillary through a closed circuit. The pumping rate was set to 20 mL/min in order to change all the tubing (1m × 2 mm) volume in less than 10 s, avoiding particle deposition on the walls. We set the camera to a sample detector distance of 1.0 m and operated at photon energy of $\lambda = 8$ keV covering the range of momentum transfer, $q = 4\pi \sin(\theta)/\lambda$, between 0.08 and 3.4 nm^{-1}. We used a Pilatus as detector with a time resolution of 5 s. Water flowing was also measured in order to assess and subtract the background from the data. The resulting two-dimensional images were radially integrated to obtain a 1D pattern of normalized intensity versus scattering vector q.

Conflict of Interest: The authors declare no competing financial interest.

Acknowledgment. C.G.S. (Centro Grandi Strumenti, Università di Cagliari) is gratefully acknowledged for use of the HRTEM facilities. Thanks are due to MIUR (Italian Ministry of University and Research) for grants to A. Ardu.

Supporting Information Available: SAXS profiles; additional XRD and TEM images. The Supporting Information is available free of charge on the ACS Publications website at DOI: 10.1021/acsnano.5b02145.

REFERENCES AND NOTES

1. Gu, D.; Schüth, F. Synthesis of Non-Siliceous Mesoporous Oxides. *Chem. Soc. Rev.* **2014**, *43*, 313–344.
2. Zhang, D.; Qi, L. Synthesis of Mesoporous Titania Networks Consisting of Anatase Nanowires by Templating of Bacterial Cellulose Membranes. *Chem. Commun.* **2005**, 2735–2737.
3. Dong, A.; Ren, N.; Tang, Y.; Wang, Y.; Zhang, Y.; Hua, W.; Gao, Z. General Synthesis of Mesoporous Spheres of Metal Oxides and Phosphates. *J. Am. Chem. Soc.* **2003**, *125*, 4976–4977.
4. Inagaki, S.; Guan, S.; Ohsuna, T.; Terasaki, O. An Ordered Mesoporous Organosilica Hybrid Material with a Crystal-like Wall Structure. *Nature* **2002**, *416*, 304–307.
5. Zhong, Z.; Subramanian, A. S.; Highfield, J.; Carpenter, K.; Gedanken, A. From Discrete Particles to Spherical Aggregates: A Simple Approach to the Self-Assembly of Au Colloids. *Chem. - Eur. J.* **2005**, *11*, 1473–1478.
6. Lin, G.; Wang, Y.; Zhang, Q.; Zhang, X.; Ji, G.; Ba, L. Controllable Formation and TEM Spatial Visualization of Cross-Linked Gold Nanoparticle Spherical Aggregates. *Nanoscale* **2011**, *3*, 4567–4570.
7. Zhong, Z.; Chen, F.; Subramanian, A. S.; Lin, J.; Highfield, J.; Gedanken, A. Assembly of Au Colloids into Linear and Spherical Aggregates and Effect of Ultrasound Irradiation on Structure. *J. Mater. Chem.* **2006**, *16*, 489.
8. Naka, K.; Itoh, H.; Chujo, Y. Self-Organization of Spherical Aggregates of Palladium Nanoparticles with a Cubic Silsesquioxane. *Nano Lett.* **2002**, *2*, 1183–1186.
9. Ewers, T. D.; Sra, A. K.; Norris, B. C.; Cable, R. E.; Cheng, C.-H.; Shantz, D. F.; Schaak, R. E. Spontaneous Hierarchical Assembly of Rhodium Nanoparticles into Spherical Aggregates and Superlattices. *Chem. Mater.* **2005**, *17*, 514–520.
10. Jia, B.; Gao, L. Morphological Transformation of Fe 3 O 4 Spherical Aggregates from Solid to Hollow and Their Self-Assembly under an External Magnetic Field. *J. Phys. Chem. C* **2008**, *112*, 666–671.
11. Yu, B. Y.; Kwak, S.-Y. Assembly of Magnetite Nanocrystals into Spherical Mesoporous Aggregates with a 3-D Wormhole-like Pore Structure. *J. Mater. Chem.* **2010**, *20*, 8320.
12. Zhu, Y.; Zhao, W.; Chen, H.; Shi, J. A Simple One-Pot Self-Assembly Route to Nanoporous and Monodispersed Fe 3 O 4 Particles with Oriented Attachment Structure and Magnetic Property. *J. Phys. Chem. C* **2007**, *111*, 5281–5285.
13. Euliss, L. E.; Grancharov, S. G.; O'Brien, S.; Deming, T. J.; Stucky, G. D.; Murray, C. B.; Held, G. a. Cooperative Assembly of Magnetic Nanoparticles and Block Copolypeptides in Aqueous Media. *Nano Lett.* **2003**, *3*, 1489–1493.
14. Xie, X.; Shen, W. Morphology Control of Cobalt Oxide Nanocrystals for Promoting Their Catalytic Performance. *Nanoscale* **2009**, *1*, 50–60.
15. Cannas, C.; Ardu, A.; Musinu, A.; Peddis, D.; Piccaluga, G. Spherical Nanoporous Assemblies of Iso-Oriented Cobalt Ferrite Nanoparticles: Synthesis, Microstructure, and Magnetic Properties. *Chem. Mater.* **2008**, *20*, 6364–6371.
16. Cannas, C.; Ardu, A.; Peddis, D.; Sangregorio, C.; Piccaluga, G.; Musinu, A. Surfactant-Assisted Route to Fabricate CoFe2O4 Individual Nanoparticles and Spherical Assemblies. *J. Colloid Interface Sci.* **2010**, *343*, 415–422.
17. Laureti, S.; Varvaro, G.; Testa, a M.; Fiorani, D.; Agostinelli, E.; Piccaluga, G.; Musinu, a; Ardu, a; Peddis, D. Magnetic Interactions in Silica Coated Nanoporous Assemblies of CoFe2O4 Nanoparticles with Cubic Magnetic Anisotropy. *Nanotechnology* **2010**, *21*, 315701.
18. Feltin, N.; Pileni, M. P. New Technique for Synthesizing Iron Ferrite Magnetic Nanosized Particles. *Langmuir* **1997**, *13*, 3927–3933.
19. Machala, L.; Zboril, R.; Gedanken, A. Amorphous iron(III) Oxide: a Review. *J. Phys. Chem. B* **2007**, *111*, 4003–4018.
20. Vestal, C. R.; Zhang, Z. J.; R. Vestal, C. Magnetic Spinel Ferrite Nanoparticles from Microemulsions. *Int. J. Nanotechnol.* **2004**, *1*, 240–263.
21. Vargas, J. M.; Zysler, R. D. Tailoring the Size in Colloidal Iron Oxide Magnetic Nanoparticles. *Nanotechnology* **2005**, *16*, 1474–1476.
22. Hyeon, T.; Lee, Su Seong; Park, J.; Chung, Y.; Na, Hyon Bin Synthesis of Highly Crystalline and Monodisperse Maghemite Nanocrystallites without a Size-Selection Process. *J. Am. Chem. Soc.* **2001**, *123*, 12798–12801.
23. Mathew, D. S.; Juang, R. S. An Overview of the Structure and Magnetism of Spinel Ferrite Nanoparticles and Their Synthesis in Microemulsions. *Chem. Eng. J.* **2007**, *129*, 51–65.
24. Cara, C.; Musinu, A.; Mameli, V.; Ardu, A.; Niznansky, D.; Buršík, J.; Scorciapino, A. M.; Manzo, G.; Cannas, C. Dialkylamide as Both Capping Agent and Surfactant in a Direct Solvothermal Synthesis of Magnetite and Titania Nanoparticles. *Cryst. Growth Des.* **2015**, *15*, 150326083956008.
25. Peddis, D.; Orrù, F.; Ardu, A.; Cannas, C.; Musinu, A.; Piccaluga, G. Interparticle Interactions and Magnetic

Anisotropy in Cobalt Ferrite Nanoparticles: Influence of Molecular Coating. *Chem. Mater.* **2012**, *24*, 1062–1071.
26. Russo, R.; Granata, C.; Esposito, E.; Peddis, D.; Cannas, C.; Vettoliere, a. Nanoparticle Magnetization Measurements by a High Sensitive Nano-Superconducting Quantum Interference Device. *Appl. Phys. Lett.* **2012**, *101*, 1–5.
27. Xia, H. B.; Yi, J.; Foo, P. S.; Liu, B. Facile Fabrication of Water-Soluble Magnetic Nanoparticles and Their Spherical Aggregates. *Chem. Mater.* **2007**, *19*, 4087–4091.
28. Grzelczak, M.; Altantzis, T.; Goris, B.; Pe, J.; Sa, A.; Bals, S.; Tendeloo, G. Van; Donaldson, S. H.; Chmelka, B. F. Hydrophobic Interactions Modulate Self-Assembly of Nanoparticles. *ACS Nano* **2012**, 11059–11065.
29. Romannikov, V. N.; Fenelonov, V. B.; Nosov, A. V.; Derevyankin, A. Y.; Tsybulya, S. V.; Kolomiichuk, V. N. Mechanism of the Formation of Porous Silicate Mesophases. *Kinet. Catal.* **2000**, *41*, 108–115.
30. Suber, L.; Plunkett, W. R. Formation Mechanism of Silver Nanoparticle 1D Microstructures and Their Hierarchical Assembly into 3D Superstructures. *Nanoscale* **2010**, *2*, 128–133.
31. Yang, H. G.; Zeng, H. C. Preparation of Hollow Anatase TiO 2 Nanospheres via Ostwald Ripening. *J. Phys. Chem. B* **2004**, *108*, 3492–3495.
32. Li, Z.; Li, L.; Yuan, Q.; Feng, W.; Xu, J.; Sun, L.; Song, W.; Yan, C. Sustainable and Facile Route to Nearly Monodisperse Spherical Aggregates of CeO 2 Nanocrystals with Ionic Liquids and Their Catalytic Activities for CO Oxidation. *J. Phys. Chem. C* **2008**, *112*, 18405–18411.
33. Jin, J.; Iyoda, T.; Cao, C.; Song, Y.; Jiang, L. Self Assembly of Uniform Spherical Aggregates of Magnetic Nanoparticles through $\Pi-\pi$ Interactions. *Angew. Chem.* **2001**, *113*, 2193–2196.
34. He, T.; Chen, D.; Jiao, X. Controlled Synthesis of Co 3 O 4 Nanoparticles through Oriented Aggregation. *Chem. Mater.* **2004**, *16*, 737–743.
35. Hou, Y.; Gao, S.; Ohta, T.; Kondoh, H. Towards 3-D Spherical Self-Assembly by Ternary Surfactant Combinations: The Case of Magnetite Nanoparticles. *Eur. J. Inorg. Chem.* **2004**, *2004*, 1169–1173.
36. Boal, A. K.; Ilhan, F.; Derouchey, J. E.; Thurn-albrecht, T.; Russell, T. P.; Rotello, V. M. Self-Assembly of Nanoparticles into Structured Spherical and Network Aggregates. *Nature* **2000**, *404*, 746–748.
37. Campi, G.; Mari, A.; Amenitsch, H.; Pifferi, A.; Cannas, C.; Suber, L. Monitoring Early Stages of Silver Particle Formation in a Polymer Solution by and Time Resolved Small Angle X-Ray Scattering. *Nanoscale* **2010**, *2*, 2447–2455.
38. Campi, G.; Mari, A.; Pifferi, A.; Amenitsch, H.; Fratini, M.; Suber, L. Control of Silver-Polymer Aggregation Mechanism by Primary Particle Spatial Correlations in Dynamic Fractal-like Geometry. *Nanoscale* **2011**, *3*, 3774–3779.
39. Liu, Z.; Ma, R.; Osada, M.; Takada, K.; Sasaki, T. Selective and Controlled Synthesis of R - and -Cobalt Hydroxides in Highly Developed Hexagonal Platelets. *J. Am. Chem. Soc.* **2005**, *127*, 13869–13874.
40. Polyakov, Y.; Goldt, E.; Sorkina, T.; Perminova, I. V.; Pankratov, D. a.; Goodilin, E.; Tretyakov, Y. D. Constrained Growth of Anisotropic Magnetic Δ-FeOOH Nanoparticles in the Presence of Humic Substances. *CrystEngComm* **2012**, *14*, 8097.
41. Cornell, R. M.; Schwertmann, U. *The Iron Oxydes: Structure, Properties, Reactions, Occurences and Uses*; Wiley-VCH: 2003; pp. ISBN: 3-527-30274-3.
42. Chen, P.; Xu, K.; Li, X.; Guo, Y.; Zhou, D.; Zhao, J.; Wu, X.; Wu, C.; Xie, Y. Ultrathin Nanosheets of Feroxyhyte: A New Two-Dimensional Material with Robust Ferromagnetic Behavior. *Chem. Sci.* **2014**, *5*, 2251.
43. Narayanan, J.; Abdul Rasheed, S.; Bellare, J. R. A Small-Angle X-Ray Scattering Study of the Structure of Lysozyme-Sodium Dodecyl Sulfate Complexes. *J. Colloid Interface Sci.* **2008**, *328*, 67–72.
44. Baxter, R. J. Percus−Yevick Equation for Hard Spheres with Surface Adhesion. *J. Chem. Phys.* **1968**, *49*, 2770.
45. Coleman, T.; Li, Y. An Interior Trust Region Approach for Nonlinear Minimization Subject to Bounds. *SIAM J. Optim.* **1996**, *6*, 418–445.
46. Coleman, T. F. On the Convergence of Interior-Reflective Newton Methods for Nonlinear Minimization Subject to Bounds. *Math. Program.* **1994**, *67*, 189–224.
47. Suber, L.; Campi, G.; Pifferi, A.; Andreozzi, P.; Mesa, C.; Amenitsch, H.; Cocco, R.; Plunkett, W. R. Polymer-Assisted Synthesis of Two-Dimensional Silver Meso-Structures. *J. Phys. Chem. C* **2009**, *113*, 11198–11203.